

A KEPLERIAN DISK AROUND ORION SrcI, A $\sim 15 M_{\odot}$ YSO

ADAM GINSBURG,¹ JOHN BALLY,² CIRIACO GODDI,^{3,4} RICHARD PLAMBECK,⁵ AND MELVYN WRIGHT⁵

¹*Jansky fellow of the National Radio Astronomy Observatory, 1003 Lopezville Rd, Socorro, NM 87801 USA*

²*CASA, University of Colorado, 389-UCB, Boulder, CO 80309*

³*ALLEGRO/Leiden Observatory, Leiden University, PO Box 9513, 2300 RA Leiden, the Netherlands*

⁴*Department of Astrophysics/IMAPP, Radboud University Nijmegen, PO Box 9010, 6500 GL Nijmegen, the Netherlands*

⁵*Radio Astronomy Laboratory, University of California, Berkeley, CA 94720*

ABSTRACT

We report ALMA long-baseline observations of Orion Source I (SrcI) with resolution 0.03-0.06'' (12-24 AU) at 1.3 and 3.2 mm. We detect both continuum and spectral line emission from SrcI's disk. We also detect a central weakly resolved source that we interpret as a hot spot in the inner disk, which may indicate the presence of a binary system. The high angular resolution and sensitivity of these observations allow us to measure the outer envelope of the rotation curve of the H₂O 5_{5,0} – 6_{4,3} line, which gives a mass $M_I \approx 15 \pm 2 M_{\odot}$. We detected several other lines that more closely trace the disk, but were unable to identify their parent species. Using centroid-of-channel methods on these other lines, we infer a similar mass. These measurements solidify SrcI as a genuine high-mass protostar system and support the theory that SrcI and the Becklin Neugebauer Object were ejected from the dynamical decay of a multiple star system ~ 500 years ago, an event that also launched the explosive molecular outflow in Orion.

arXiv:1804.10622v1 [astro-ph.GA] 27 Apr 2018

1. INTRODUCTION

Orion Source I (SrcI) is the closest candidate forming high-mass ($M > 8 M_{\odot}$) star, and as such is the most important protostar for testing basic theories of how massive stars form. However, despite its relative proximity at a mere ≈ 415 pc from the sun (Menten et al. 2007; Kim et al. 2008), the mass of SrcI has been the subject of prolonged debate, with several estimates putting its mass below the classic $8 M_{\odot}$ threshold for a single star to go supernova (Heger et al. 2003).

Several attempts have been made to measure the mass of Orion SrcI using the rotation curve of various molecular lines:

- Kim et al. (2008) used 3D VLBI measurements of SiO masers to infer a source mass $M = 8M_{\odot}$.
- Matthews et al. (2010) used 3D VLBI measurements of SiO masers to infer a mass $M \approx 8 - 10 M_{\odot}$.
- Hirota et al. (2014) observed H_2O emission from the $v_2 = 0, 10_{2,9} - 9_{3,6}$ and $v_2 = 1, 5_{2,3} - 6_{1,6}$ lines. They made velocity centroid maps of the position of peak intensity as a function of velocity to measure the rotationally supported mass in SrcI. They obtained a mass estimate of $5 - 7 M_{\odot}$ using a model of a simple uniform ring orbiting at Keplerian velocity.
- Plambeck & Wright (2016) measured both the continuum SED and the rotation curve of gas around SrcI. They used a centroiding and modeling approach similar to Hirota et al. (2014) to measure the rotation curve of SiO and vibrationally excited CO and infer the source mass $M \sim 5 - 7 M_{\odot}$.
- Hirota et al. (2017) used Si^{18}O J=12-11 to infer a mass $M = 8.7$ using a similar approach to Hirota et al. (2014) and Plambeck & Wright (2016).

SrcI’s mass is an important parameter in models of the origin of the Orion Outflow. Several authors argue that SrcI, BN, and SrcN (or, alternatively, SrcX; Luhman et al. 2017) were part of a single non-hierarchical multiple system that underwent dynamical decay, and this decay somehow triggered the outflow (Bally & Zinnecker 2005; Rodríguez et al. 2005; Goddi et al. 2011; Moeckel & Goddi 2012; Bally et al. 2011, 2015, 2017; Rodríguez et al. 2017). However, others have noted that the lower masses inferred for SrcI above are incompatible with this scenario (Chatterjee & Tan 2012; Plambeck & Wright 2016; Farias & Tan 2017), which requires a

mass $M_I \gtrsim 15 M_{\odot}$. An alternative scenario is described in which BN was ejected from the Trapezium and had a close encounter with SrcI that triggered the outflow (Tan 2008a,b; Chatterjee & Tan 2012). A third alternative, that the outflow is driven by many independent sources (Beuther & Nissen 2008), is disfavored by the overall symmetry of the outflow (Bally et al. 2017).

We present new measurements of SrcI’s mass, finding it has $M_I \sim 15 M_{\odot}$. In Section 2, we present details of the observations. In Section 3, we discuss measurements of the continuum and spectral lines. Section 4 discusses these results and some of their simple physical implications. We conclude in Section 5. Several appendices present additional figures and detailed method discussion.

2. OBSERVATIONS

Observations were taken with two configurations in each of Band 3, 6, and 7 at ALMA as part of project 2016.1.00165.S. The epochs and broad details about the configuration are given in Table 1. The multiconfiguration data were combined for all images considered here. The flux and phase calibrators are listed in Table 1. Band 7 data are not discussed in this work because the data for the long-baseline observations were not delivered by the time of submission; we record the observational details here for completeness since they are part of the same project in the ALMA archive.

Continuum images were produced with several weighting parameters to emphasize different scales, though most of the discussion here will be limited to the robust -2 weighted images with the highest resolution. The calibrated data delivered from the ALMA QA2 process were imaged directly, since we found that self-calibration did not improve the image; we suspect the unmodeled, resolved-out emission prevents us from obtaining good calibration solutions.

To emphasize the disk scales and eliminate ripple artifacts produced by poorly-sampled large-scale structure in the map, we used data only from baselines > 150 m (115 k λ , angular scales $< 1.8''$) in the robust -2 images used for disk fitting and modeling.

The continuum images have dynamic range in the vicinity of SrcI of about 200-400. These values are reported in Table 2 and are measured by taking the ratio of the peak intensity in SrcI to the standard deviation within a neighboring, apparently signal-free region (an $r = 0.7''$ circle $1.4''$ to the northwest of SrcI).

Spectral line image cubes were produced covering the complete data set to identify lines associated with the disk. Cubes were produced centered on SrcI with robust 0.5 and -2 weightings. These cubes were only

Table 1. Observation Summary

Date	Band	Array	Observation Duration seconds	Baseline Length Range meters	# of antennae	FluxCal	PhaseCal
08-Oct-2016	6	12m	2332	17-3144	43	J0522-3627	J0541-0541
31-Oct-2016	7	12m	2671	19-1124	42	J0522-3627	J0532-0307
19-Sep-2017	6	12m	5556	41-12147	42	J0522-3627	J0541-0541
24-Sep-2017	3	12m	5146	21-12147	41	J0423-0120	J0541-0541
25-Sep-2017	3	12m	5180	41-14854	42	J0423-0120	J0541-0541

Table 2. Continuum Image Parameters

Band	Robust	Beam Major "	Beam Minor "	Beam PA °	T_B/S_ν 10^3 K Jy $^{-1}$	RMS mJy beam $^{-1}$	Source I $S_{\nu,max}$ mJy beam $^{-1}$	Dynamic Range
B6	-2	0.037	0.022	67.0	30.3	0.087	19.638	220
B3	-2	0.065	0.041	50.9	53.2	0.038	14.179	370

cleaned in the $0.5'' \times 0.5''$ region immediately surrounding SrcI, therefore lines with significant emission from the surrounding medium may be significantly affected by sidelobes. Continuum-subtracted cubes were produced by subtracting the median across the 1.8 GHz bandwidth in each spectral window. All cube analysis was performed using `spectral-cube` (<https://spectral-cube.readthedocs.io/en/latest/>).

Relevant parameters of the cubes are described in Table 3. For the noise estimate, we use the median absolute deviation (MAD) to estimate the standard deviation over the full continuum-subtracted cutout cube, which effectively ignores the few channels that have significant line emission (the directly-measured standard deviation and MAD-estimated standard deviation differ by $< 5\%$).

Cutouts of the data used for the analysis in this work along with the software and scripts used for the analysis are presented at <https://zenodo.org/record/1213350>.

3. RESULTS

3.1. Continuum

We detect the disk in the continuum at 3.2 mm, 1.3 mm, and 0.8 mm (Figure 1 shows the 3.2 and 1.3 mm images¹). At 1.3 mm, where we have enough resolution to clearly distinguish the line-emitting region from the disk midplane, we detect spectral lines only from the surfaces above and below the continuum disk (Figure

2). The nondetection of lines in the disk midplane is a strong indication that the continuum is optically thick, as has previously been noted (e.g., [Plambeck & Wright 2016](#)).

We fit the highest-resolution 1.3 mm and 3.2 mm continuum image with a simple model to determine the basic observational structure. The optimization was performed using a Levenberg-Marquardt fitter ([Newville et al. 2014](#)). We used a linear model (i.e., an infinitely thin perfectly edge-on disk) for the disk, with endpoints and amplitude as free parameters. This simple model left significant residuals, so we added a two-dimensional Gaussian smoothing kernel as another three free parameters to obtain a substantially better fit. The models and their residuals are shown in Appendix A.

We determined that the disk is resolved in both directions, with a vertical FWHM height of about 20 AU and a length of about 100 AU (Table 4). These measurements are close to those published by [Plambeck & Wright \(2016\)](#), though their data only marginally resolved the source at wavelengths 1.3 mm and shorter.

This simple model leaves a significant residual compact source near the center of the disk, which we measured by adding a smeared point source to the model (see Appendix A). We have allowed the source to be smeared only in the direction of the disk’s elongation, requiring only two additional free parameters. This source is discussed further in Section 4.6.

Table 4 lists the fitted parameters. It includes measurements of the total integrated intensity recovered in the model and the ratio of the compact central source to the total. We also display fits to the [Reid et al. \(2007\)](#)

¹At the time of submission, the long-baseline 0.8 mm data products had not been delivered, so they are excluded from the analysis presented here.

Table 3. Line Cube Parameters

Band	SPW	Freq. Range GHz	Robust	Beam Major "	Beam Minor "	Beam PA °	RMS mJy beam ⁻¹	RMS K	Channel Width km s ⁻¹
B3	0	85.463-87.337	-2	0.066	0.043	45.0	2.5	144.8	3.4
B3	1	87.358-89.232	-2	0.064	0.050	41.5	2.5	121.1	3.3
B3	2	97.462-99.336	-2	0.061	0.039	45.8	2.0	108.4	3.0
B3	3	99.358-101.232	-2	0.060	0.038	45.3	2.3	122.2	2.9
B6	0	229.168-231.042	-2	0.026	0.022	64.0	2.8	115.9	1.3
B6	1	231.835-233.709	-2	0.026	0.021	61.6	3.1	125.0	1.3
B6	2	214.277-216.151	-2	0.027	0.023	62.8	3.2	131.5	1.4
B6	3	216.976-218.850	-2	0.030	0.023	55.2	3.2	120.5	1.3
B3	0	85.463-87.337	0.5	0.101	0.072	40.6	0.8	17.3	3.4
B3	1	87.358-89.232	0.5	0.098	0.080	40.3	0.7	15.0	3.3
B3	2	97.462-99.336	0.5	0.091	0.060	43.6	0.7	16.8	3.0
B3	3	99.358-101.232	0.5	0.081	0.058	39.6	0.7	18.2	2.9
B6	0	229.168-231.042	0.5	0.043	0.035	-88.1	0.9	14.6	1.3
B6	1	231.835-233.709	0.5	0.043	0.034	-87.4	1.0	15.7	1.3
B6	2	214.277-216.151	0.5	0.046	0.037	-88.7	1.2	18.2	1.4
B6	3	216.976-218.850	0.5	0.049	0.039	72.7	1.0	14.1	1.3

7 mm continuum data with the same model; these fits do not contain any absolute astrometry information.

The disk position angle points to within 2 degrees of the Becklin-Neugebauer object (Orion BN); the PA of the vector from SrcI to Source BN is -37.6 degrees, while the measured disk position angle is -36 to -37 degrees. This coincidence was noted by [Bally et al. \(2011\)](#) and [Goddi et al. \(2011\)](#).

The disk has a peak brightness temperature at 1.3 mm of ~ 600 K at the position of the compact source and $\sim 400 - 500$ K at other positions, with a gradual decline from the center to the exterior. These measurements agree with the continuum model of [Plambeck & Wright \(2016\)](#), who inferred the presence of an optically thick $T = 500$ K surface from the SED. The 3.2 mm continuum has a higher peak brightness temperature at the position of the central compact source, but otherwise is consistent with the 1.3 mm brightness (see Figure 1).

3.2. SiO Lines

We detect several SiO lines, including the 1 mm ²⁸SiO $v=0$ and $v=1$ J=5-4 lines, the the 3 mm isotopologue lines ²⁹SiO $v=0$ and $v=1$ J=2-1, and the 3 mm ²⁸SiO $v=0$ and $v=1$ J=2-1 lines. Several of these transitions are known and well-studied masers. Some images of these data are shown in Appendix B, but because the emphasis of this work is not on the outflow, we do not discuss the SiO further here.

3.3. Water Line

The next brightest line after the masing SiO lines is the H₂O $5_{5,0} - 6_{4,3}$ line at 232.68670 GHz, with $E_U = 3461.9$ K. [Hirota et al. \(2012\)](#) detected this line in 2" resolution ALMA Science Verification data, but believed it to be masing. We report here that, because it is similar in morphology and excitation level to the 336 GHz vibrationally excited water line reported in [Hirota et al. \(2014\)](#), and it has a peak brightness temperature $\sim 1500 \pm 100$ K (in the robust -2 maps; see Figure 2), it is most likely a thermal line.

The water line traces an X-shaped feature above and below the disk, resembling the overall distribution of SiO masers. The water is not directly aligned with the continuum disk (Figures 2 and 19), but it does exhibit emission parallel to the disk at small (< 20 AU) separation. The morphology of this line confirms that it traces both the disk and the inner rotating outflow discussed by [Hirota et al. \(2017\)](#) (see also [Kim et al. 2008](#); [Matthews et al. 2010](#)).

Because the water emission is thermal, it exhibits less extreme brightness fluctuations across the image than the SiO masers, allowing us to fit an upper-envelope velocity curve in Section 3.5. The kinematics of the water line away from the disk are discussed further in Appendix C.

3.4. Other lines

Table 4. Continuum Fit Parameters

Frequency	Disk FWHM	Disk Radius	Disk PA	Pt RA	Pt Dec	Pt Amp	Pt Width	Pt Flux	Total Flux	Pt %
GHz	AU	AU	°	s	"	mJy	AU	mJy	mJy	
43.165	25 ± 0.44	41 ± 1.1	-36	-	-	1.00 ± 0.01	16 ± 0.69	3	10	29%
93.3	17 ± 0.09	37 ± 0.71	-38	0.518	-0.0405	2.00 ± 0.03	9.4 ± 0.38	5.7	57	10%
224.0	21	51 ± 0.78	-37	0.518	-0.0409	3.20	23	15	280	5.5%

The pointlike source position is given as RA seconds and Dec arcseconds offset from ICRS 5h35m14s -5d22m30s. The error on this position is 0.003s (RA) and 0.0003" (Dec). For the 7 mm data, the position is left blank because we do not have astrometric information for those data (they were self-calibrated on a bright maser whose position was not well-constrained).

The disk FWHM is the vertical full-width half-maximum of the fitted Gaussian profile. No formal parameter errors were measured for several of the 224.0 GHz fitted quantities because of a linear algebra failure in the fitter; the errors are likely similar to the 93.3 GHz fit errors. The Pt Flux and Total Flux columns report the integrals of the best-fit models.

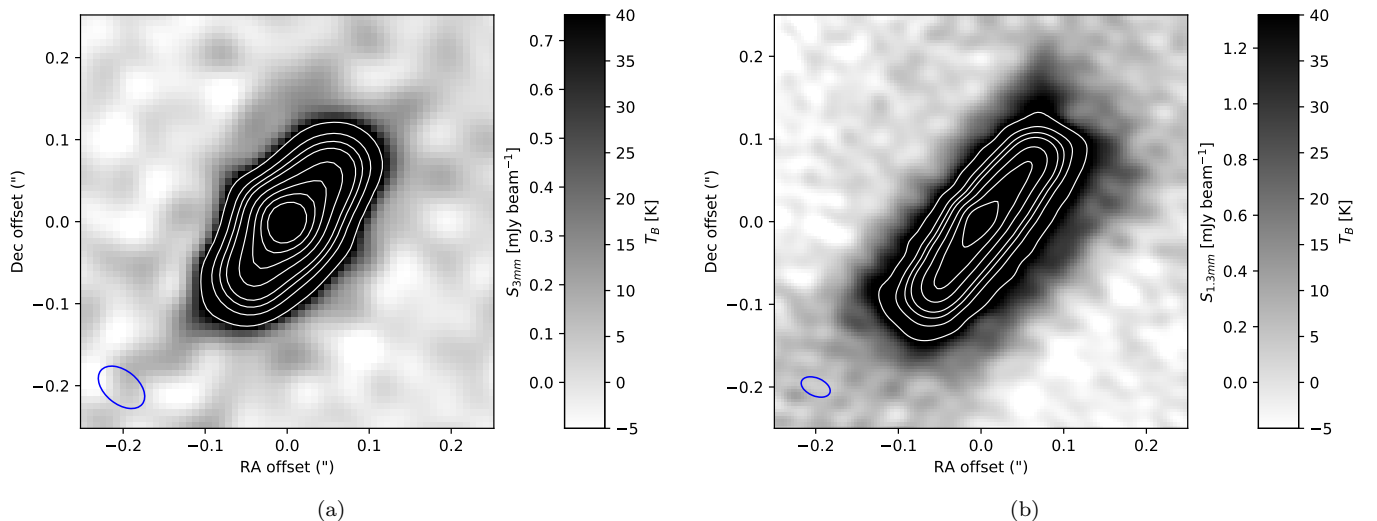


Figure 1. The robust -2 continuum image of Orion Src I at 3.2 mm (left) and 1.3 mm (right). The beam is shown in the bottom left, with size $0.065'' \times 0.041''$ at PA= 50.9° (3.2 mm, left) and $0.037'' \times 0.022''$ at PA= 67° (1.3 mm, right). Contours are overlaid at $T_B = 50, 100, 150, 200, 300, 400,$ and 500 K. The displayed coordinates are offsets from ICRS 05:35:14.5172 -05:22:30.612 (3.2 mm) and ICRS 05:35:14.5173 -05:22:30.6135 (1.3 mm).

Several unidentified lines are observed in emission at the outer edge of the continuum disk. A table of their approximate rest frequencies is presented in Appendix D. They all share a common morphology, though they vary in strength. The peak signal from these lines appears around the $T_B \sim 150$ K contour in the robust -2 weighted 1.3 mm continuum images (Figure 2), and the lines are particularly strong at the endpoints of the disk. Little line emission is detected where the continuum is brightest, $T_B \gtrsim 300$ K.

The best explanation for these lines is that they trace the outer surface of a mostly optically thick (in the continuum) disk. In this scenario, the lines have an excitation temperature similar to the brightness temperature of the disk, but have optical depths of order $\tau \sim 0.1-1$. Directly toward the disk continuum emission peak, since the line excitation temperature is the same

as the background continuum temperature, $T_{ex} = T_{bg}$, no emission (or absorption) is observed. Just above and below the disk midplane continuum peak, the dust column density (and therefore optical depth) drops rapidly, but the molecular optical depth drops more slowly, so some emission is still observed ($T_{ex} \sim 200 - 500$ K, but $\tau_{line} \sim 0.1 - 0.5$, resulting in the $T_{B,max} \sim 100$ K observed). At the disk endpoints, the column density of molecular material is higher because we are looking along the tangent of the disk, so the line optical depth and therefore brightness are greater.

Since these lines only appear immediately around the disk, and in particular because they peak just outside of the dust emission along the disk axis, they are the most direct tracers of the disk's kinematics.

3.5. Kinematics: a Keplerian disk

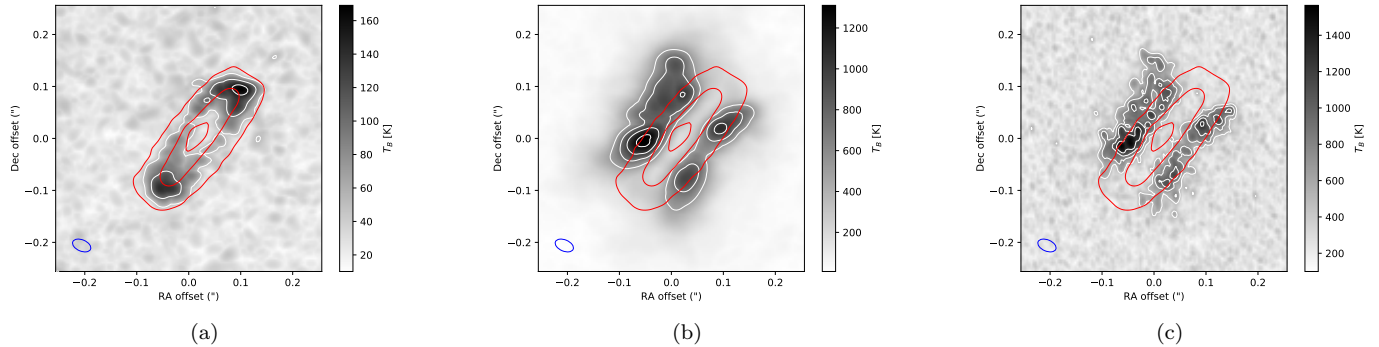


Figure 2. Peak intensity map of an unknown line (U230.322; left) and the H_2O line (middle, right) with continuum overlaid in red contours at levels of 50, 300, and 500 K. White contours are shown at 50, 100, and 150 K (left), and 500, 750, 1000, and 1250 K (middle, right). The H_2O and unknown line clearly trace different physical structures, as they exhibit no coincident emission peaks. The water line does not exhibit emission directly along the disk midplane. The left two figures are robust 0.5 weighted images, while the right is a robust -2 weighted image with higher resolution and poorer sensitivity. The U230.322 line is not detected in the robust -2 cubes. The positions shown are offsets from coordinate ICRS 05:35:14.5184 -05:22:30.6194.

The disk appears to exhibit a Keplerian rotation curve, which allows us to use the velocity profile to measure the central mass. Following Seifried et al. (2016), we measure the outer edge of the detected emission in a position-velocity (PV) diagram to define the rotation curve surrounding Src1. The emission along each line-of-sight in the PV diagram is followed from its peak down to some emission threshold. We use a threshold of $5\text{-}\sigma$, as was done in Seifried et al. (2016), but we also assess the importance of this threshold in Section 3.5.2. Additionally, to facilitate direct comparison with previous works, we use the centroid-of-velocity-channel approach in Appendix E (although Seifried et al. (2016) warn it may underestimate the central mass) and obtain similar results, albeit from different spectral lines.

Of the detected lines, the H_2O line spans the widest range of velocities as a function of radius. As shown in Figure 3, there is H_2O emission spanning at least radii $r \approx 10$ to 100 AU. Many other molecules, most of which we have not been able to identify, span a range of radii 30-80 AU, while SiS spans 30 AU to an unconstrained outer radius. The SiO lines span varying radii, but they are predominantly detected far from the disk midplane (however, see Appendix B, in which SiO also exhibits Keplerian velocity curves).

We find that a $15 M_\odot$ edge-on Keplerian rotation curve fits² the outer edge of the H_2O line well (Figure 3). The $15 M_\odot$ profile is also an acceptable match to the outer profiles of the unidentified lines described in Sec-

²We do not report best-fit parameters and statistical errors here because the errors on the outer envelope are poorly characterized and likely dominated by systematic errors such as channel discretization.

tion 3.4 and shown in supplemental figures in Appendix F.

A lower-mass central source is consistent with the H_2O data only if we allow for substantial line broadening driven by turbulence. We estimate an upper limit on the turbulent line broadening of $FWHM \lesssim 4 \text{ km s}^{-1}$ based on the narrowest features observed in the H_2O and other unknown lines, which results in a one-sided broadening of $HWHM < 2 \text{ km s}^{-1}$; if such line-broadening is present, the mass may be lower by $\sim 20 - 30\%$. However, since Flaherty et al. (2017) observe stringent upper limits on turbulence in lower-mass disks, we expect turbulent broadening to be relatively small, and possibly negligible. The upper-limit line broadening we observe is both consistent with line blending from unresolved kinematics within the beam and is close to the intrinsic velocity resolution of our data.

A substantially smaller mass, such as the $5\text{-}10 M_\odot$ suggested previously (Plambeck & Wright 2016; Hirota et al. 2014), is inconsistent with the data: for models with such masses, emission is clearly detected outside of the predicted Keplerian curve (see, e.g., the green curve in Figure 3).

3.5.1. Examination of alternative velocity profile models

To support the argument that the velocity profiles are Keplerian, as opposed to some other power-law profile as has been found for the outer envelopes of several low-mass YSOs (Lee et al. 2017; Aso et al. 2017; Ohashi et al. 2014; Lindberg et al. 2014; Murillo et al. 2013), we show power-law fits to the outer envelope velocity profile of the H_2O line in Figure 4. This figure convincingly demonstrates that a power law $\alpha = 1$ (e.g., as observed in the outer parts of low-mass YSO disks; Aso et al.

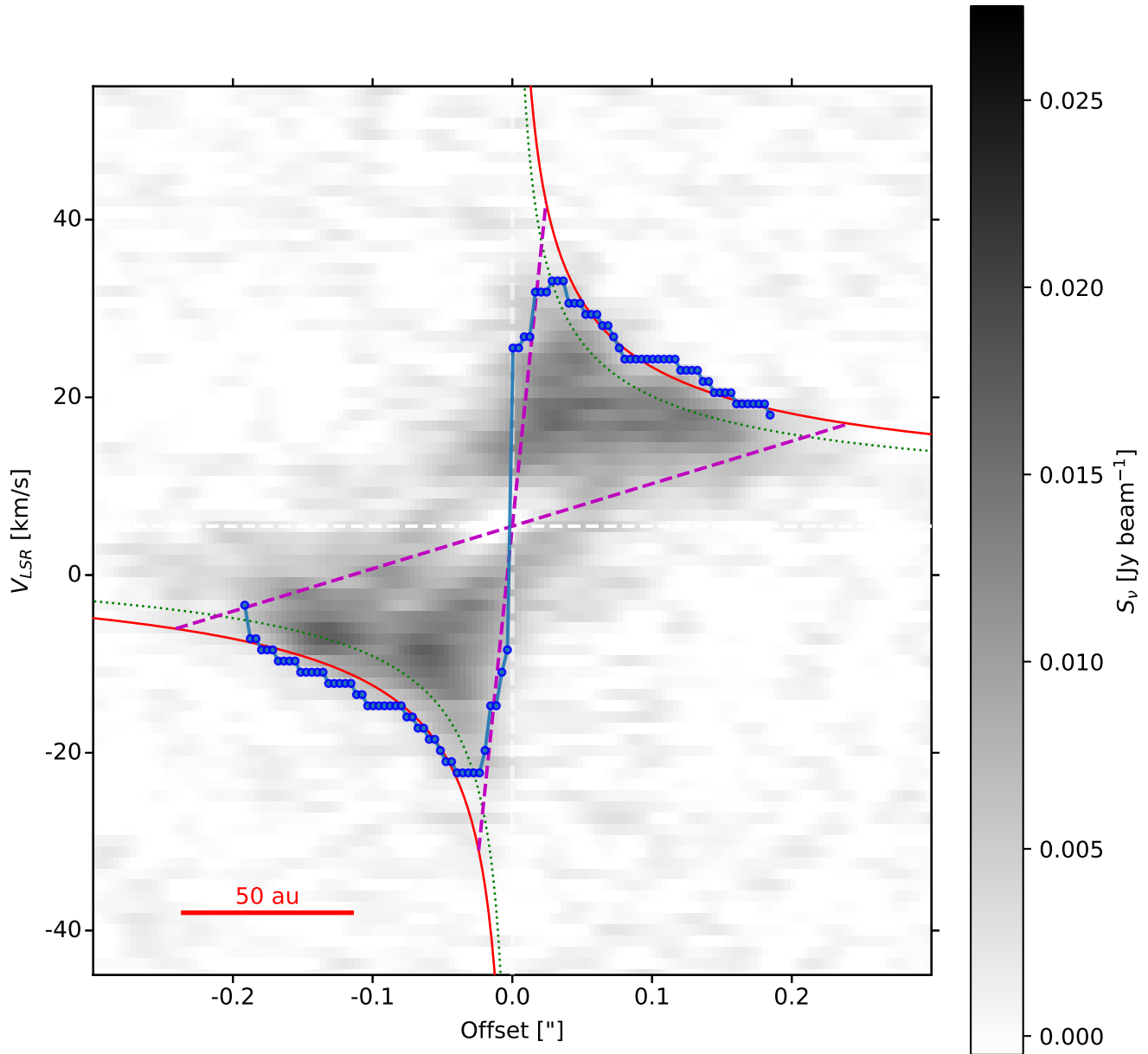


Figure 3. Position-velocity diagram of H₂O 5_{5,0} - 6_{4,3}. The colorbars show average intensity along the extracted region in units of mJy beam⁻¹. The blue line with dots is the outer envelope of the velocity curve determined using the method of Seifried et al. (2016). The red solid and green dotted curves show the Keplerian velocity profile surrounding a 15 and 10 M_\odot central source, respectively. White dashed lines indicate the adopted source central position 05h35m14.5172s -05d22m30.618s (ICRS) and central velocity (5.5 km s⁻¹). The purple dashed lines show the full orbital path for radii of 10 and 100 AU and indicate the approximate limits of the disk. This PV diagram is extracted from the midplane of the robust 0.5 image, but the emission displayed is beam-smearred from just above and below the continuum disk.

2017) is inconsistent with the data. While the best-fit profile of $\alpha \approx 0.4$ is slightly shallower than the Keplerian $\alpha = 0.5$ curve, both shallow profiles are consistent with the data. The limited spectral resolution of our data is evident in this plot, where there is little separation in velocity from $\sim 30 - 50$ AU; higher spectral resolution observations or more sophisticated modeling may be able to provide a tighter constraint on the power-law slope.

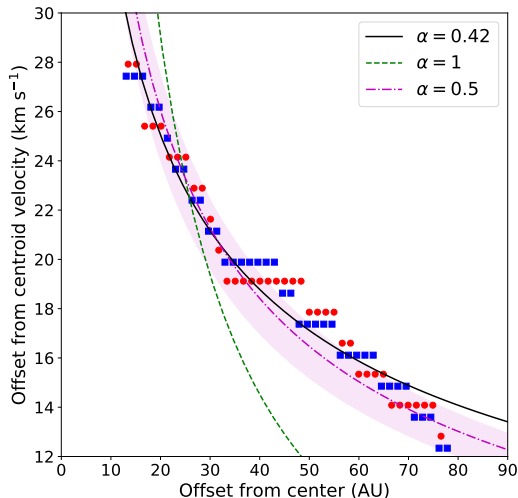


Figure 4. Radial profile of the outer-envelope velocity profile extracted from Figure 3b. The red and blue points represent the redshifted and blueshifted components of the velocity profile, respectively. The velocities are shown relative to the best-fit centroid velocity for the H_2O line, $v_{LSR} = 5.2$ km s^{-1} . The curves show the best-fit power-law (black solid line) and the best-fit curves with fixed powerlaw indices of 0.5 (magenta dotted line) and 1 (green dashed line). The magenta filled curve shows a powerlaw index $\alpha = 0.5$, i.e., a Keplerian rotation curve, for the range $13M_{\odot} < M < 17M_{\odot}$.

The mass for the $\alpha = 0.5$ curve is $M = 15 M_{\odot}$. We do not determine masses for the other models since they are not consistent with a pointlike gravitational potential. We show the curves for a central 13-17 M_{\odot} source in filled magenta: since there are many points above the curve, a more massive central source is plausible, while a less massive source is unlikely.

3.5.2. An estimate of the error on the mass measurement

We assess the uncertainty introduced by the threshold level adopted in the velocity envelope profile measurement. Figure 5 shows the effects of increasing or decreasing the threshold, which is to decrease or increase the measured mass, respectively. These figures suggest

that our measurement uncertainty with the PV envelope fitting technique is approximately $2 M_{\odot}$.

4. DISCUSSION

4.1. The mass of SrcI

We measure a mass for the object at the center of the disk of $M_I = 15 M_{\odot}$, which is higher than most measurements previously reported. Our mass measurement is higher than previous works in part because our spatial resolution is high enough to allow a direct fit of the rotation curve to the outer envelope of an emission line in position-velocity space. Additionally, though, the greater sensitivity of these observations allowed us to detect the outer envelope of the H_2O position-velocity diagram and detect - and resolve - several unknown lines that directly trace the disk. The inconsistency between these new estimates and the lower masses previously derived from SiO measurements hints that, in this system, SiO chemically selects a kinematically distinct region from the disk.

Even if SrcI consists of an equal-mass binary, this mass measurement confirms that the Orion Molecular Cloud is presently a region with ongoing high-mass star formation.

4.2. The luminosity of SrcI

Since we observe an optically thick surface, we can infer the luminosity required to keep such a surface at the observed $T_{B,1.3\text{mm}} \approx 500$ K assuming it is heated only by radiation. Taking the disk radius to be 50 AU, the required central source luminosity is $6500 L_{\odot}$. This estimate should be taken as a lower limit, since the inner disk is likely to be optically thick and capable of shielding the outer disk, thereby keeping the observed $\tau = 1$ surface at 1.3 mm cooler than would be produced by radiative equilibrium with the central star.

4.3. Properties of the disk

Our observations yield disk properties nearly identical to those in Plambeck & Wright (2016), so we do not revisit their disk mass or density estimates. We note, however, that these new observations have sufficient angular resolution to distinguish the molecular lines that trace the outflow from those that directly trace the disk.

4.4. The dynamical decay scenario

Several authors (Gómez et al. 2008; Goddi et al. 2011; Bally et al. 2011) suggested that the high proper motion of SrcI, BN, and SrcN, combined with the observed H_2 outflow, implied the outflow and the runaway stars were produced in the same single event ~ 500 years ago. That event was the dynamical decay of a non-hierarchical multiple system, i.e., it was the interaction

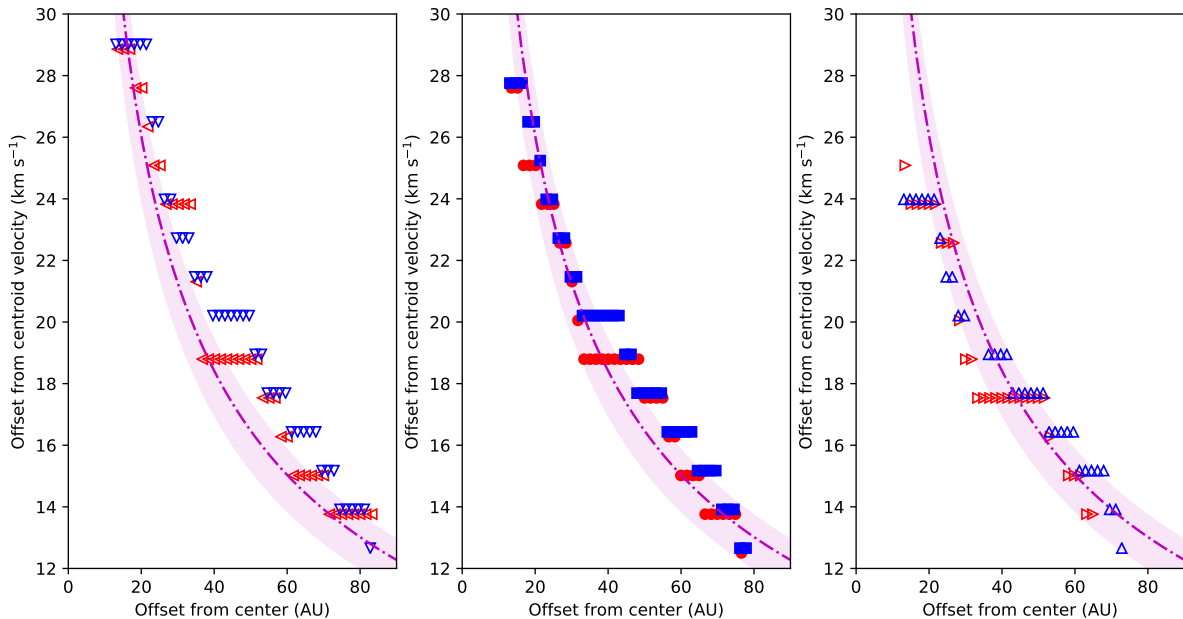


Figure 5. Demonstration of the effect of a changing threshold in the Seifried method. The panels show a lower $3\text{-}\sigma$ threshold (left), the adopted $5\text{-}\sigma$ threshold (center), and a higher $7\text{-}\sigma$ threshold (right). The magenta highlighted region is the same $13\text{-}17 M_{\odot}$ Keplerian curve shown in Figure 4.

of multiple stars at the center of a small cluster. More recent observations by Luhman et al. (2017) have shown that SrcN is unlikely to have participated in this interaction, but instead that SrcX, another star within the same field, has high proper motion that points back to the interaction center (Bally et al, in prep).

Farias & Tan (2017) report that, while any dynamical decay scenario involving Sources I, X, and BN that can reproduce the observed proper motions are unlikely, those with a higher mass for SrcI ($M_I > 14 M_{\odot}$) are the only ones capable of producing the observed proper motions³. Our observed higher mass for SrcI, $M_I \gtrsim 15 M_{\odot}$, therefore implies that the dynamical interaction scenario remains viable.

4.5. Is the disk consistent with the dynamical ejection model?

Plambeck & Wright (2016) argue that both the mass of SrcI and the presence of the disk rule out the dynamical ejection model of Bally et al. (2011). We have shown that the star is significantly more massive, but what about the disk?

³Their results are similar to those obtained in Goddi et al. (2011) and Moeckel & Goddi (2012), but now with SrcX instead of SrcN as the third member of the interaction.

Following Bally et al. (2011), we note that the disk truncates at $R < 50$ AU. At this radius, the orbital timescale is ~ 70 years, so gas at the disk’s outer radius would have had five to ten dynamical times to relax into a circular disk configuration after the explosive event.

The alignment of SrcI’s disk with the I-BN vector is consistent with a dynamical interaction between these sources. If the ejection resulted in SrcI and BN being launched in nearly opposite directions from their center of mass (which must have been moving in the rest frame of the Orion nebula; Bally et al. in prep), any material around SrcI that remained bound would be dragged in the direction of SrcI, and would therefore have a resulting angular momentum vector orthogonal to the direction of motion. Any material with velocity relative to SrcI

$$v < v_{esc} = 23 \text{ km s}^{-1} (M_I/15 M_{\odot})^{1/2} (r/50 \text{ AU})^{-1/2}$$

would remain bound. Assuming SrcI’s present-day proper motion of 11.5 km s^{-1} reflects its velocity at the time of ejection, less than half of the original disk mass would have been lost, while the rest would remain bound (material moving in the direction directly opposite SrcI’s ejection direction would have net velocity relative to SrcI high enough to escape; the greatest mass loss would occur if the disk was already in the direction of SrcI’s eventual launch). Material outside $R \gtrsim 200$

AU (where $v_I = 11.5 \text{ km s}^{-1} > v_{esc}$) would likely all have become unbound, while other material would be retained in a disk parallel to Source I's proper motion.

4.6. The compact source in the disk

We have detected a compact (but marginally resolved) source near the center of the disk at both 3.2 mm and 1.3 mm. The source has a spectral energy distribution that is shallow from 3.2 mm to 1.3 mm ($\alpha \approx 1.1$). Since the source is nearly coincident with an edge-on disk that we show is optically thick at 1.3 mm, it is likely that the source is thermal but is significantly attenuated by the disk at 1.3 mm and seen with less attenuation at 3.2 mm.

Reid et al. (2007) used comparable-resolution 7 mm VLA data to infer the presence of a 2.2 mJy source at the center of the SrcI disk. The compact-source-to-disk flux ratio at 7 mm was $\sim 30\%$, substantially higher than we observe at 1.3 mm and somewhat higher than at 3.2 mm (Table 4). The spectral index of this compact source from 7 to 3.2 mm is $\alpha = 1.6$, approaching that of an optically thick blackbody.

The central source has a surface temperature $T \geq 1250 \text{ K}$, the brightness temperature of a 2.2 mJy source within a 41×28 milliarcsecond beam at 7 mm. If the source is a 5000 K spherical blackbody (e.g., Testi et al. 2010), it must have a radius $R = 7.5 \text{ AU}$. Such a gigantic star is implausible, as it would produce a luminosity of $1.5 \times 10^6 L_\odot$, several orders of magnitude higher than the total luminosity in the region. We therefore argue that this emission source is not a star.

What is the emission mechanism from this central source? It could simply be hot, optically thick dust that is partly obscured by the cooler disk at higher frequencies. The extension of this 'source' along the disk direction (Appendix A, Figure 6) suggests that we are seeing the hot inner disk. As pointed out by Plambeck & Wright (2016), it is quite unlikely to be classical free-free emission from protons and electrons, since there are no detected recombination lines. However, it is still plausible that the emission is produced by brehmsstrahlung emission from HI and H₂ (Reid et al. 2007; Báez-Rubio et al. 2018).

The source is slightly offset from the center of the disk by $5.8 \pm 1.5 \text{ AU}$ in projection⁴. This offset, combined with the source's extent, implies that it is not a single central source, but instead is a hot region of the inner

disk. Such an asymmetry in the disk could be driven either by instability in the disk or, if the central star is a binary, by the proximity of the more luminous companion.

If this source is an inner edge of the disk, it may imply the presence of a binary that has cleared the area within $r < 6-10 \text{ AU}$. Since a tight binary is one of the expected outcomes of the dynamical interaction scenario (Goddi et al. 2011), this detection of the inner region in dust emission provides additional circumstantial evidence for that scenario.

If SrcI's central source is a binary, and the measured offset of $\sim 5 \text{ AU}$ between the disk midpoint and the central emission source is real, we can guess that the binary's orbit is $\lesssim 5 \text{ AU}$. For such an orbital radius, the orbital timescale is only ~ 3 years. It will therefore be productive to re-observe SrcI over the next several years to see if the hot spot moves on such a timescale.

5. CONCLUSIONS

We report observations that resolve SrcI's disk in both continuum and line emission. We measure the mass of SrcI by fitting the rotation curve with a Keplerian disk model, finding the following:

1. The central source has mass $M = 15 \pm 2 M_\odot$, where the error bar represents the range of consistent models rather than a typical $1 - \sigma$ statistical uncertainty.
2. The H₂O 5_{5,0} – 6_{4,3} line is not masing and kinematically traces both the upper envelope of the disk and the lower portion of the outflow.
3. We observe several lines that trace the disk kinematics directly, though the molecules producing these lines remain unidentified. These lines are visible only toward the outskirts of the disk and are morphologically distinct from both the H₂O and SiO lines that follow the outflow.
4. A compact source in the approximate center of the disk is resolved at 1.3 mm, and it is slightly off-center. It therefore is most likely a hot region of the inner disk. It may be produced by time-varying illumination from an unequal mass binary.

The mass we have measured is higher than in several recent publications because both the resolution and sensitivity of our observations were greater. These new data allowed us to identify and measure the spectral features that directly trace the disk kinematics, while previous data convolved the disk and outflow kinematics. This

⁴We measure the errors on the source position by fitting a 2D Gaussian model to an image with the disk model subtracted. While this approach yields a useful statistical error, it does not account for the systematic error introduced by fitting the disk model.

higher measured mass implies that the dynamical decay scenario for the SrcI- BN - SrcX system is viable.

We thank the anonymous referee for a thorough and helpful review. This paper makes use of the following ALMA data: ADS/JAO.ALMA#2016.1.00165.S ALMA is a partnership of ESO (representing its member states), NSF (USA) and NINS (Japan), together with NRC (Canada), MOST and ASIAA (Taiwan), and KASI (Republic of Korea), in cooperation with the Republic of Chile. The Joint ALMA Observatory is operated by ESO, AUI/NRAO and NAOJ. The National Radio Astronomy Observatory is a facility of the National Science Foundation operated under cooperative agreement by Associated Universities, Inc.

Software: The software used to make this version of the paper is available from github at https://github.com/keflavich/Orion_ALMA_2016.1.00165.S (<https://doi.org/10.5281/zenodo.1181877>) with hash 68a49ad(2018-04-26). The tools used include `spectral-cube` (<https://doi.org/10.5281/zenodo.591639> and <https://github.com/radio-astro-tools/spectral-cube>) and `radio-beam` (<https://github.com/radio-astro-tools/radio-beam>, <https://doi.org/10.5281/zenodo.1181879>) from the `radio-astro-tools` package ([radio-astro-tools.github.io](https://github.com/radio-astro-tools)), `astropy` (Astropy Collaboration et al. 2013), `astroquery` (astroquery.readthedocs.io, <https://doi.org/10.5281/zenodo.591669>) and `CASA` (McMullin et al. 2007).

REFERENCES

- Aso, Y., Ohashi, N., Aikawa, Y., et al. 2017, *ApJ*, 849, 56
- Astropy Collaboration, Robitaille, T. P., Tollerud, E. J., et al. 2013, *A&A*, 558, A33
- Bález-Rubio, A., Jiménez-Serra, I., Martín-Pintado, J., Zhang, Q., & Curiel, S. 2018, *ApJ*, 853, 4
- Bally, J., Cunningham, N. J., Moeckel, N., et al. 2011, *ApJ*, 727, 113
- Bally, J., Ginsburg, A., Arce, H., et al. 2017, *ApJ*, 837, 60
- Bally, J., Ginsburg, A., Silvia, D., & Youngblood, A. 2015, *A&A*, 579, A130
- Bally, J., & Zinnecker, H. 2005, *AJ*, 129, 2281
- Beuther, H., & Nissen, H. D. 2008, *ApJL*, 679, L121
- Chatterjee, S., & Tan, J. C. 2012, *ApJ*, 754, 152
- Farias, J. P., & Tan, J. C. 2017, ArXiv e-prints, arXiv:1712.08485
- Flaherty, K. M., Hughes, A. M., Rose, S. C., et al. 2017, *ApJ*, 843, 150
- Goddi, C., Humphreys, E. M. L., Greenhill, L. J., Chandler, C. J., & Matthews, L. D. 2011, *ApJ*, 728, 15
- Gómez, L., Rodríguez, L. F., Loinard, L., et al. 2008, *ApJ*, 685, 333
- Heger, A., Fryer, C. L., Woosley, S. E., Langer, N., & Hartmann, D. H. 2003, *ApJ*, 591, 288
- Hirota, T., Kim, M. K., & Honma, M. 2012, *ApJL*, 757, L1
- Hirota, T., Kim, M. K., Kurono, Y., & Honma, M. 2014, *ApJL*, 782, L28
- Hirota, T., Machida, M. N., Matsushita, Y., et al. 2017, ArXiv e-prints, arXiv:1712.04606
- Kim, M. K., Hirota, T., Honma, M., et al. 2008, *PASJ*, 60, 991
- Lee, C.-F., Li, Z.-Y., Ho, P. T. P., et al. 2017, *ApJ*, 843, 27
- Lindberg, J. E., Jørgensen, J. K., Brinch, C., et al. 2014, *A&A*, 566, A74
- Luhman, K. L., Robberto, M., Tan, J. C., et al. 2017, *ApJL*, 838, L3
- Matthews, L. D., Greenhill, L. J., Goddi, C., et al. 2010, *ApJ*, 708, 80
- McMullin, J. P., Waters, B., Schiebel, D., Young, W., & Golap, K. 2007, in *Astronomical Society of the Pacific Conference Series*, Vol. 376, *Astronomical Data Analysis Software and Systems XVI*, ed. R. A. Shaw, F. Hill, & D. J. Bell, 127
- Menten, K. M., Reid, M. J., Forbrich, J., & Brunthaler, A. 2007, *A&A*, 474, 515
- Moeckel, N., & Goddi, C. 2012, *MNRAS*, 419, 1390
- Murillo, N. M., Lai, S.-P., Bruderer, S., Harsono, D., & van Dishoeck, E. F. 2013, *A&A*, 560, A103
- Newville, M., Stensitzki, T., Allen, D. B., & Ingarciola, A. 2014, *LMFIT: Non-Linear Least-Square Minimization and Curve-Fitting for Python*, , , doi:10.5281/zenodo.11813. <https://doi.org/10.5281/zenodo.11813>
- Ohashi, N., Saigo, K., Aso, Y., et al. 2014, *ApJ*, 796, 131
- Plambeck, R. L., & Wright, M. C. H. 2016, *ApJ*, 833, 219
- Reid, M. J., Menten, K. M., Greenhill, L. J., & Chandler, C. J. 2007, *ApJ*, 664, 950
- Rodríguez, L. F., Dzib, S. A., Loinard, L., et al. 2017, *ApJ*, 834, 140
- Rodríguez, L. F., Poveda, A., Lizano, S., & Allen, C. 2005, *ApJL*, 627, L65
- Seifried, D., Sánchez-Monge, Á., Walch, S., & Banerjee, R. 2016, *MNRAS*, 459, 1892

Tan, J. C. 2008a, in *Astronomical Society of the Pacific Conference Series*, Vol. 387, *Massive Star Formation: Observations Confront Theory*, ed. H. Beuther, H. Linz, & T. Henning, 346

Tan, J. C. 2008b, *ArXiv e-prints*, arXiv:0807.3771

Testi, L., Tan, J. C., & Palla, F. 2010, *A&A*, 522, A44

APPENDIX

A. CONTINUUM MODELING FIGURES

In this appendix, we show figures illustrating the continuum modeling process. Figures 6 and 7 show the model and residuals for the band 6 and band 3 data, highlighting the significantly improved fit as more model parameters are added.

In Figure 6, the apparent point sources at the edge of the disk in the central column are artificial features introduced by the model; since the model is forced to be smooth, the best-fit model is one that is more centrally peaked, which results in an under-prediction of the disk brightness toward the edges.

Also in this figure, there appears to be a faint ‘halo’ of emission at the ~ 30 K level around the modeled region. The halo is asymmetric, with a greater extent toward the southwest. If this feature is not an artifact of the data reduction, which we cannot rule out, it is likely to be from optically thin dust above and below the disk, since it is not detected in the 3.2 mm data.

B. THE SiO OUTFLOW IN PV SPACE

To illustrate the change in velocity structure with height from the disk, we show position-velocity diagrams of SiO $v=0$ J=5-4 in Figure 8 and ^{29}SiO J=5-4 in Figure 9. These images are extracted from equal distances above and below the disk midplane. At greater distances from the midplane, the high-velocity, low-separation features fade out, while more low-velocity material becomes visible at larger separations. These structures are similar to what was shown in the 484 GHz Si^{18}O J=12-11 line in Figure 2 of Hirota et al. (2017). Our data are consistent with their interpretation that the SiO isotopologues trace a rotating, expanding outflow. In the innermost slice, which shows the SiO emission that just skirts the edges of the disk, the velocity curve is consistent with the $15 M_{\odot}$ Keplerian curve overlaid.

C. A DEEPER EXAMINATION OF THE WATER LINE: EVIDENCE THAT IT TRACES THE DISK KINEMATICS

The H_2O -derived mass presented in Section 3.5 relies on the H_2O line tracing the disk kinematics. Since the H_2O clearly also traces the outflow, showing the same X-shaped morphology as the SiO, it does not trace just the disk.

Nonetheless, the midplane position-velocity slice of the H_2O line does appear to genuinely trace disk kinematics. Qualitatively, the PV diagram appears exactly as expected for a disk with an inner and out radial cutoff.

To assess possible contamination from the outflow, we compare position velocity slices at different vertical displacements from the disk center in Figure 10. The left panel shows the kinematic signature we attribute to the disk, which closely resembles that predicted for a pure Keplerian rotation curve. In contrast, the middle panel is likely dominated by outflow emission, since it shows material $0.05\text{-}0.1''$ (20-40 AU) above the disk, i.e., just outside the $1\text{-}\sigma$ height of the continuum disk. While the outflow continues to show some motion similar to that of the disk, it lacks the characteristic convex shape of a Keplerian orbit at higher velocities and separation. Finally, the rightmost panel shows that the water emission nearly disappears at heights $h > 0.1'' = 40$ AU while the maximum velocities observed get smaller ($dv < 10 \text{ km s}^{-1}$), suggesting that rotation slows in the outflow.

Figure 10 also characterizes some of the ‘forbidden’ velocity components, i.e., those seen in quadrants 2 and 4. These components get stronger at higher vertical positions on the disk, implying that they come from the outflow, not the disk. The “ring” shape observed in the high-latitude figures indicates the outflow is expanding (see, e.g., the model in supplementary figure 1 of Hirota et al. 2017). The velocity asymmetry, which shows an excess toward the red side of the disk and outflow, is also present in SiO. We do not have a straightforward explanation for this asymmetry except to assert that it implies an asymmetry in the direction of mass ejection in the outflow. These velocity components are unlikely to be produced by infall motions, since they are observed perpendicular to the disk along the direction of the outflow.

D. STACKED SPECTRA

We reported the detection of several unidentified lines. To measure their frequencies precisely, we performed a stacking analysis in which we adopt the velocity field of the U232.511 line, shift all spectra across the disk to the same velocity frame, and average them. We stacked the robust 0.5 cubes, as the surface brightness sensitivity of the robust -2 cubes was too poor to justify stacking. We then fit the lines with Gaussians to determine their centroid frequency. We searched within a narrow range of velocities ($v_{LSR} = 3 - 8 \text{ km s}^{-1}$) for known lines in the Splatalogue

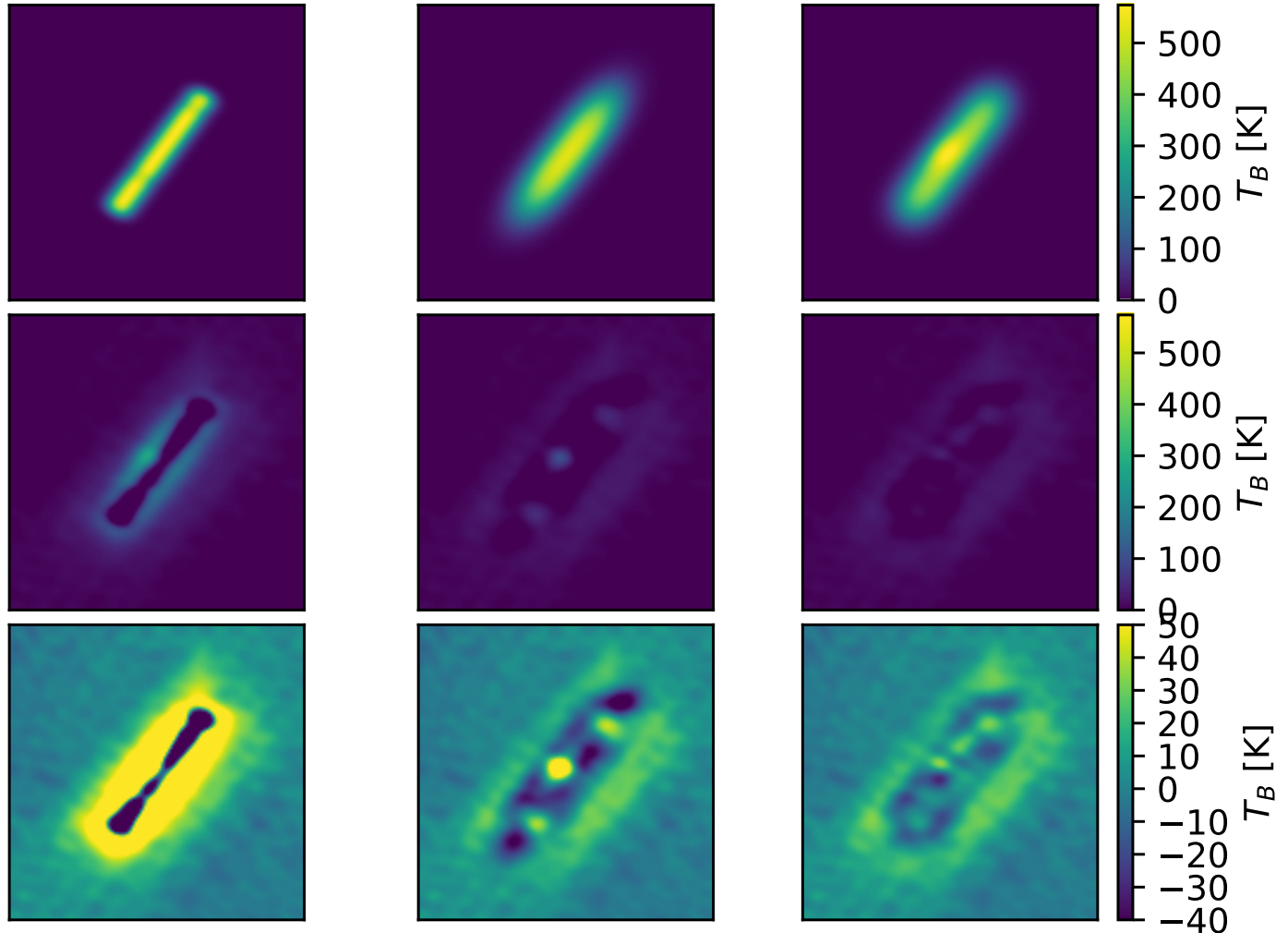


Figure 6. A series of plots showing the band 6 continuum models used and their residuals. The top row shows the models, starting from a simple 1D linear model convolved with the beam (left), continuing with a disk smoothed with a broader beam to account for scale height (middle), and finally a version of the middle model with a smeared point source added (right). The fit parameters are given in Table 4. The second and third row show the residuals (data - model) for each of the models in the top row; the bottom row uses a narrow linear scale to emphasize the lower-amplitude residuals, while the top two use an arcsinh stretch to display the full dynamic range.

collection of line catalogs using `astroquery`. While many of the lines have plausible carriers within $1\text{-}2\text{ km s}^{-1}$, such as highly-excited CH_3OCHO or variants of SO_2 , there is no consistent pattern to the detected lines and no individual species can explain more than a few of the observed lines. These disk-averaged spectra are shown in Figure 12 with the lines labeled.

We list the line frequencies (which we use as line names), fitted Gaussian widths, and fitted amplitudes from the stacked spectra in Table 5.

E. DISK PARAMETER DETERMINATION METHOD COMPARISON

To compare fairly with Hirota et al. (2014) and Plambeck & Wright (2016), we used the centroid-velocity method to measure the central source mass. In this approach, we fit two-dimensional Gaussian profiles to each ‘blob’ in each velocity channel in the PPV cubes of spectral lines. Unlike previous works, we have had to fit multiple Gaussians in several channels, since we resolve the structure and see ‘blobs’ both above and below the disk. Figures 13, 14, and 15 show the results of this analysis.

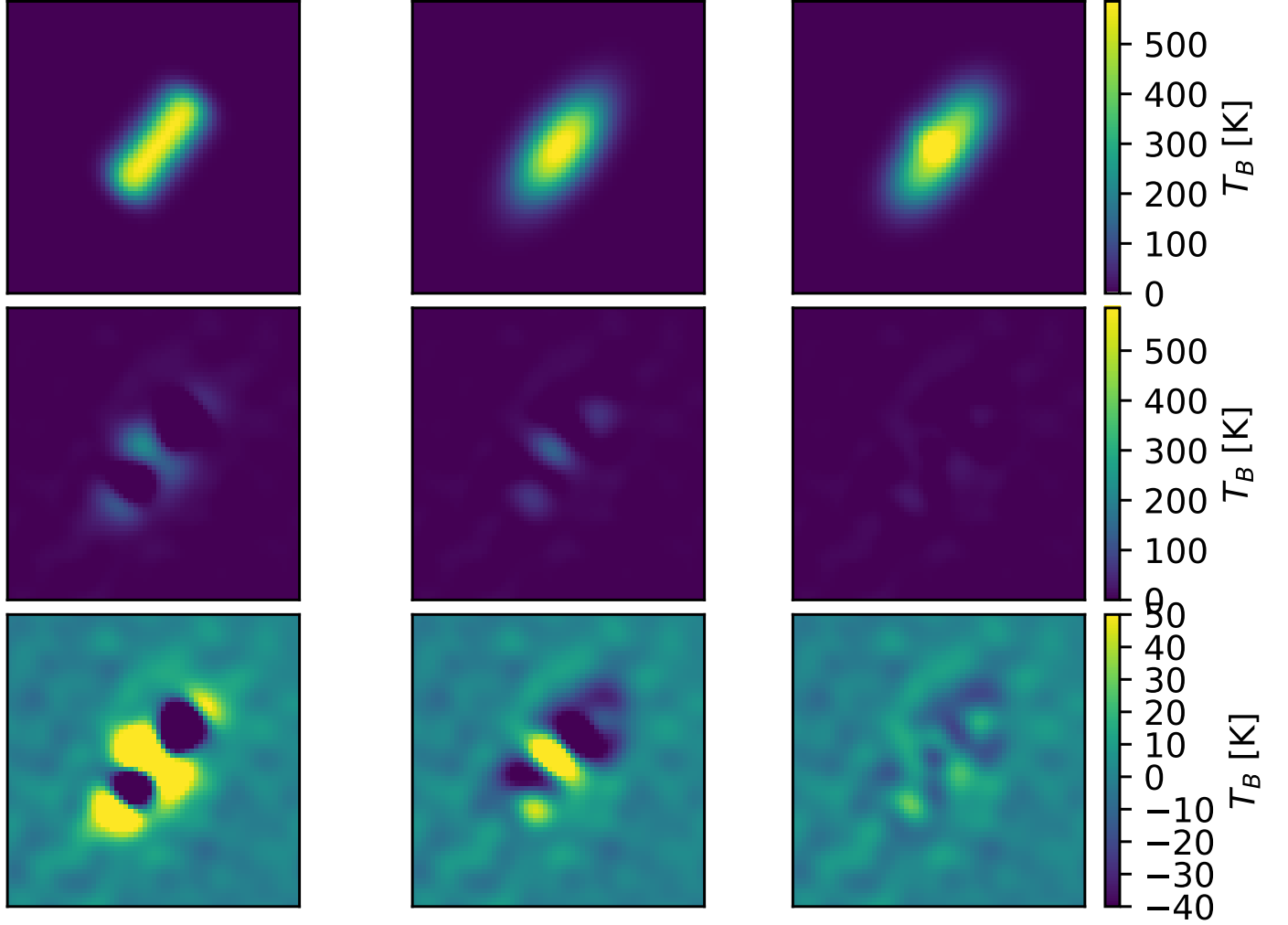


Figure 7. A series of plots showing the band 3 continuum models used and their residuals. See the caption of Figure 6 for details.

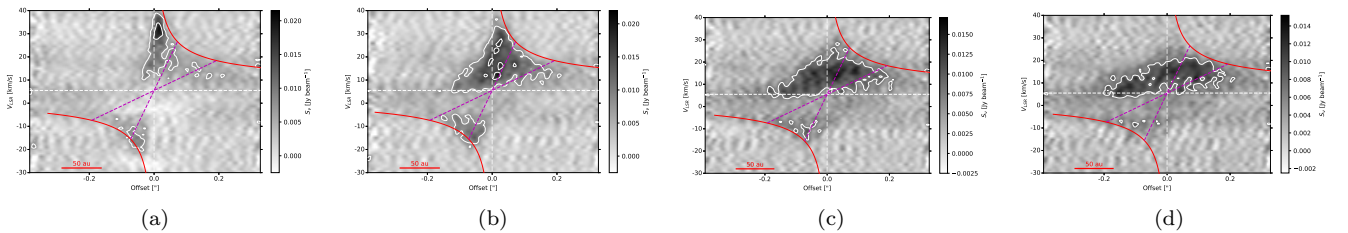


Figure 8. Position-velocity slices of SiO $v=0$ $J=5-4$ along the disk direction at four heights: (a) $|h| < 0.05''$, (b) $0.05'' < |h| < 0.1''$, (c) $0.1'' < |h| < 0.15''$, (d) $0.15'' < |h| < 0.2''$. Contours are overlaid at 5 and 10 σ . These images are produced from the robust -2 weighted cubes. The missing emission around $v = 0$ km s $^{-1}$ is likely caused by image filtering effects; at these velocities, there is extended, smooth SiO emission from the surrounding cloud.

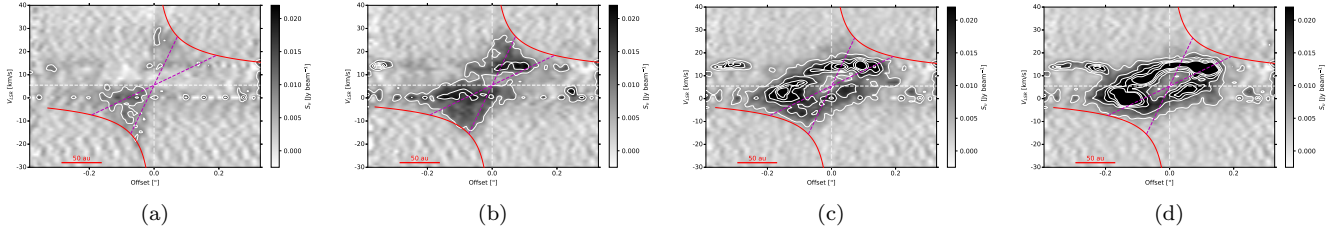


Figure 9. Position-velocity slices of $^{29}\text{SiO } v=0 \text{ J}=5-4$ along the disk direction at four heights: (a) $|h| < 0.05''$, (b) $0.05'' < |h| < 0.1''$, (c) $0.1'' < |h| < 0.15''$, (d) $0.15'' < |h| < 0.2''$. Contours are overlaid at 5, 10, 15, 20, and 25 σ . These images are produced from the robust -2 weighted cubes. While similar to the ^{28}SiO shown in Figure 8, there is a remarkable position-velocity ring at high elevations that is coincident with many of the SiO and H_2O masers.

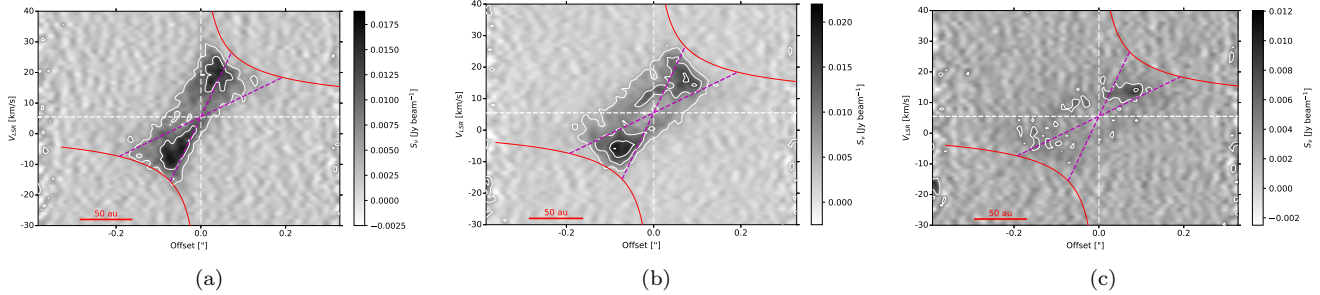


Figure 10. Position-velocity slices of the $\text{H}_2\text{O } 5_{5,0} - 6_{4,3}$ line at different heights above the disk plane from the robust -2 data cube. The left panel shows the inner $0.1''$ (i.e., near the midplane, $|h| < 0.05''$, $|h| < 20 \text{ AU}$), the middle shows the range $0.05'' < |h| < 0.1''$, and the right shows the range $0.1'' < |h| < 0.15''$. All three panels show averages over the specified range, with the colorbar showing intensity in mJy beam^{-1} . Contours are overlaid at 5, 10, 15, and 20 σ . The red solid lines show the Keplerian profile for a $15 M_\odot$ central source, and the purple dashed lines show the orbital track for a particle at 30 and 80 AU for such a source; these are included primarily to guide the eye. The middle and right panel are dominated by the outflow, while the left panel is dominated by the Keplerian orbital profile.

We have modeled the velocity profile assuming an edge-on, uniform, optically thin disk with a sharp central hole and outer truncation. Position-velocity curves derived with this approach are shown in the above figures. Figure 16 shows the curves for a range of masses and radii. This model approach is the same used by Plambeck & Wright (2016). We fit this model to the centroid data points. The fits were performed on the *average* positional offset at each velocity, since for many velocities there were two or more Gaussian components fitted in the image. The mass, inner and outer radius, and centroid velocity were left as free parameters. The fit results are shown in the legend of Figures 13 and 14; in Figure 15, we show only a fiducial model because the best-fit model did not describe the data well.

The positions of the fitted components are significantly different for each species, which helps illustrate why previous estimates of SrcI’s mass were low. Fits to both the SiO line in Figure 14 and water in Figure 15 have lower masses than the fit to the U232.511 line in Figure 13 that more closely traces the disk.

In the edge-on disk models, different inner-radius cutoffs have an effect on the inner velocity profile slope similar to changing the central mass, so it is likely that the disk parameters, rather than the central source mass, dominate our uncertainties in this approach. Figure 16 demonstrates this effect: the inner slope of a $5 M_\odot$, $20 \text{ AU} < r < 50 \text{ AU}$ disk is indistinguishable from a $20 M_\odot$, $30 \text{ AU} < r < 80 \text{ AU}$ disk, though the latter extends to higher velocity and radius.

E.1. A demonstration of issues with the centroid-of-velocity method

Figure 17 shows an example of how the centroid-of-velocity approach produces lower mass fits for some lines, particularly H_2O and SiO. The figure shows both the optically thin edge-on disk model and the midplane-extracted position-velocity diagram with overlaid centroid fits. The centroid fits notably do not extend nearly as far as emission is visible. This discrepancy results from the midplane emission being much fainter than some of the off-plane emission.

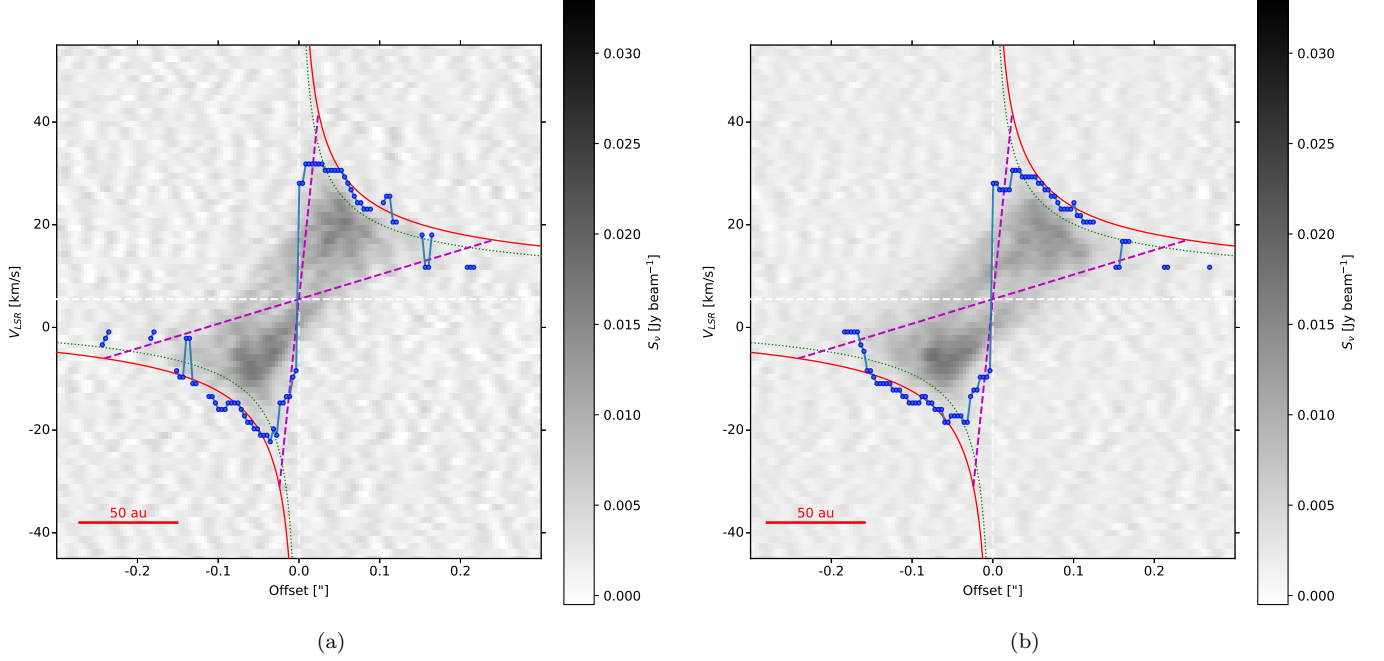


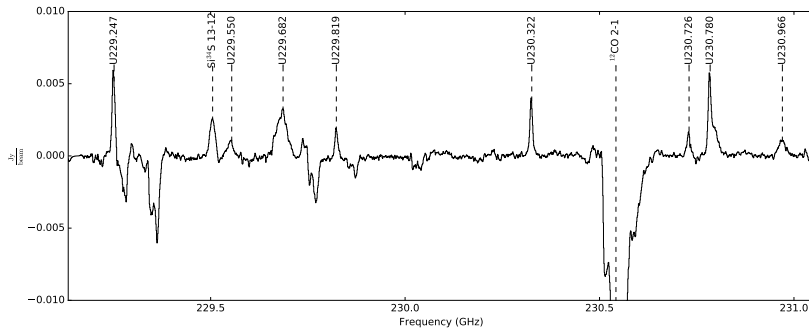
Figure 11. Duplicate of Figure 3 for robust -2 data with different vertical extents included in the position-velocity slice. The left figure shows the average PV slice over the vertical range range $h = \pm 0.05''$, and the right right shows the same with $h = \pm 0.1''$.

By contrast, a similar side-by-side comparison of the edge-on optically thin model with the U232.511 line reveals a better match. In Figure 18, the overall structure of the observed position-velocity diagram is well-matched to the model.

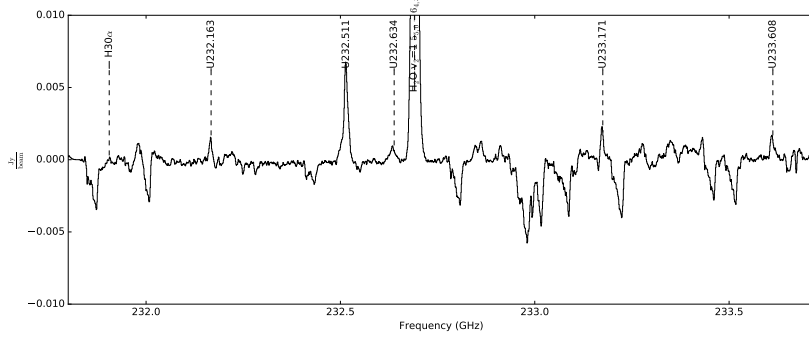
F. ADDITIONAL FIGURES SHOWING THE DISK

We include several additional figures showing the disk moment 0 maps and position-velocity profiles for some other unknown lines. These figures show that the lines displayed in the main text are not unique.

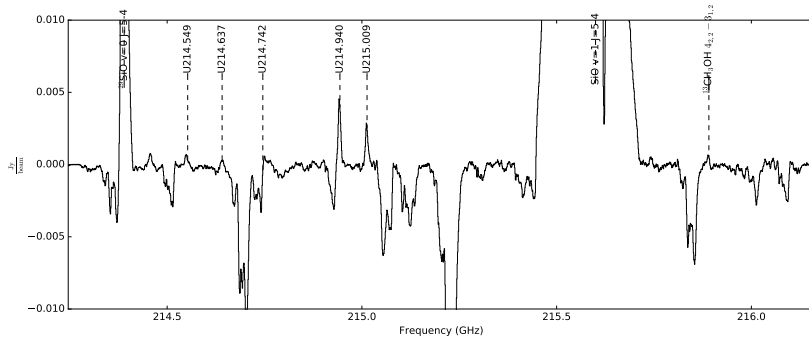
Figure 19 shows moment 0 maps, which provide a slightly different view from the peak intensity maps shown in Figure 2. Figures 20 and 21 show peak intensity, moment 0, and position-velocity maps of the U232.511 and U217.980 lines.



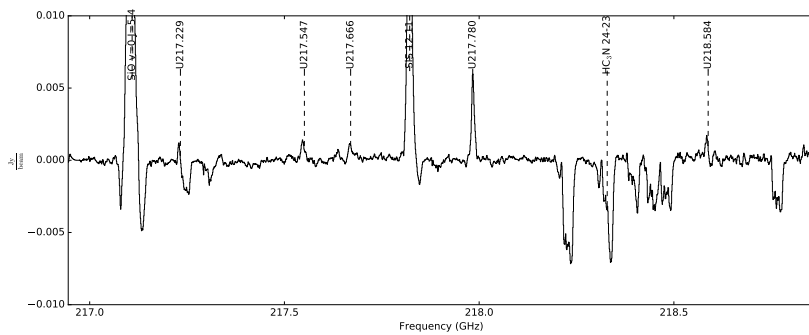
(a)



(b)



(c)



(d)

Figure 12. Plots of the stacked spectra from spectral windows 0, 1, 2, and 3 (see Table 3) with detected lines labeled. The spectra are shown with the same y-axis limits; bright SiO and H₂O emission is cut off. In spectral window 2, the region around 215.5-215.6 GHz, near the SiO v=1 J=5-4 maser line (which is the brightest line we detect) is affected by imaging artifacts from the cleaning process.

Table 5. Unknown Line Frequencies

Line Name	Frequency GHz	Fitted Width km s^{-1}	Fitted Amplitude mJy
U214.549	214.549	4.1	0.7
U214.637	214.637	3.2	0.3
U214.742	214.742	-	-
U214.940	214.940	4.3	4.6
U215.009	215.009	4.6	2.7
U217.229	217.229	2.6	1.3
U217.547	217.547	6.8	1.2
U217.666	217.666	7.2	1.1
U217.980	217.980	5.2	5.6
U218.584	218.584	4.5	1.6
U229.247	229.247	4.8	5.9
U229.550	229.550	8.0	1.1
U229.682	229.682	15.5	3.0
U229.819	229.819	4.7	1.8
U230.322	230.322	4.7	3.8
U230.726	230.726	5.8	1.5
U230.780	230.780	6.7	5.1
U230.966	230.966	10.4	1.1
U232.163	232.163	4.2	1.5
U232.511	232.511	6.7	6.2
U232.634	232.634	7.8	0.8
U233.171	233.171	4.2	2.3
U233.608	233.608	6.8	1.5

The frequencies listed have a systematic uncertainty of about 2 km s^{-1} (1.5 MHz) because they are referenced to the U232.511 line, which has an unknown rest frequency. The rest frequency used for the U232.511 line was selected to maximize the symmetry of the emission around 5 km s^{-1} . Some lines were detected in only part of the disk and therefore had bad or malformed profiles in the stacked spectrum; these have fits marked with '-s'.

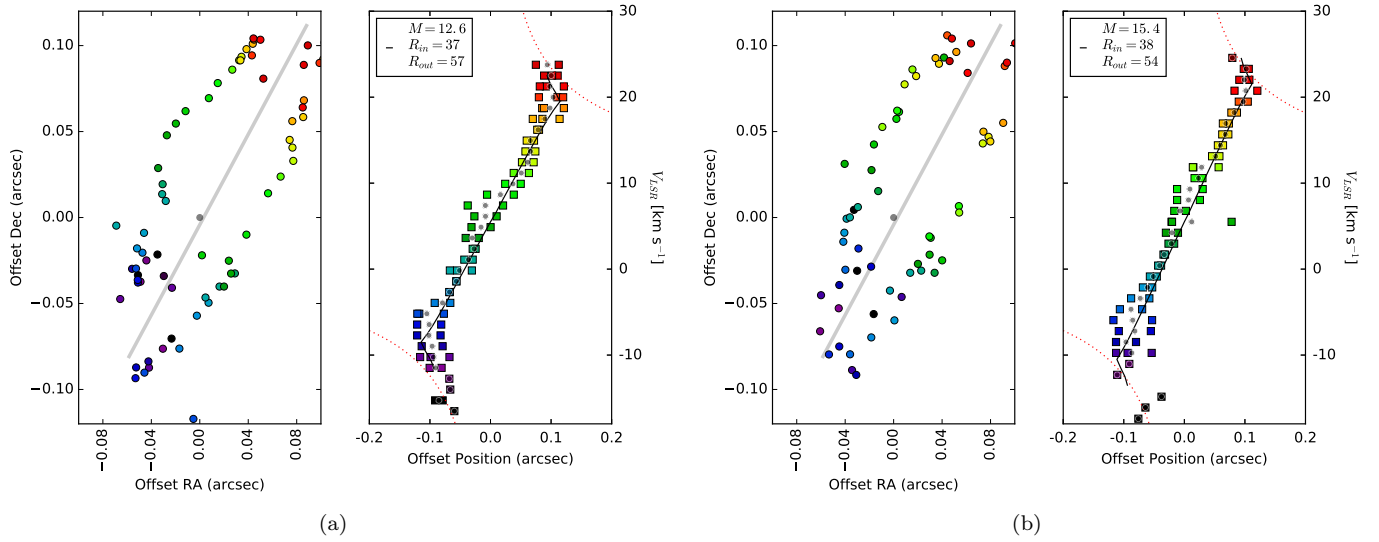


Figure 13. Results of the centroid-velocity analysis for the U232.511 line (left) and the U230.322 line (right). The left panel shows the locations of fitted centroids in the position-position plane relative to the midpoint of the disk. The position of the central compact source is marked with a grey circle at the center. The grey line indicates the disk midplane as determined from the continuum modeling. The circles are colored by their velocity as indicated in the right panel. The right panel shows a position-velocity diagram of these same centroids. The dotted external curves show Keplerian velocity profiles for a $15 M_{\odot}$ (red solid) central source; this curve does *not* represent what should be observed in a centroid-of-velocity plot. The black curve shows the predicted centroid velocity profile of an optically-thin edge-on disk with parameters displayed in the figure.

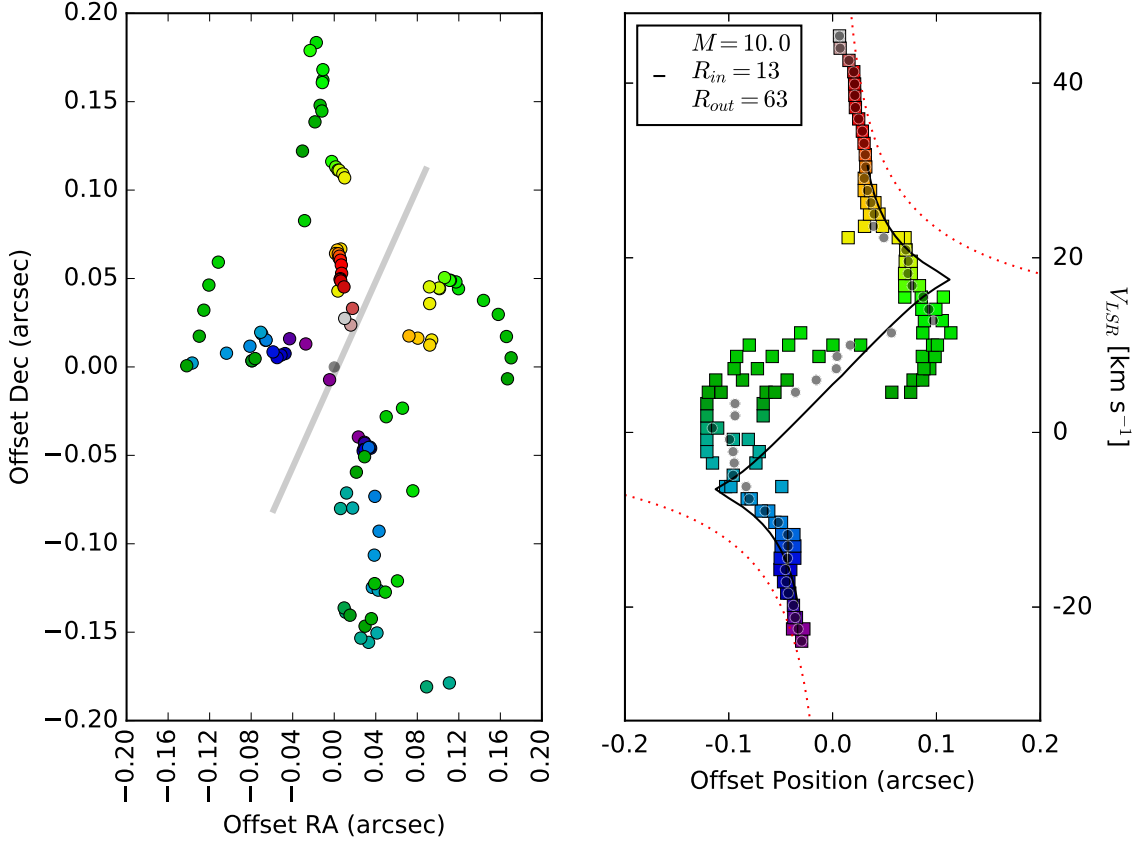


Figure 14. Results of the centroid-velocity analysis for the SiO $v=1$ $J=5-4$ line. See Figure 13 for details. Note that the data are inconsistent with the disk model; the SiO emission fitted here traces the bottom of the outflow and possibly some components of the disk upper atmosphere. The average positions at each velocity are closer to a reasonable fit.

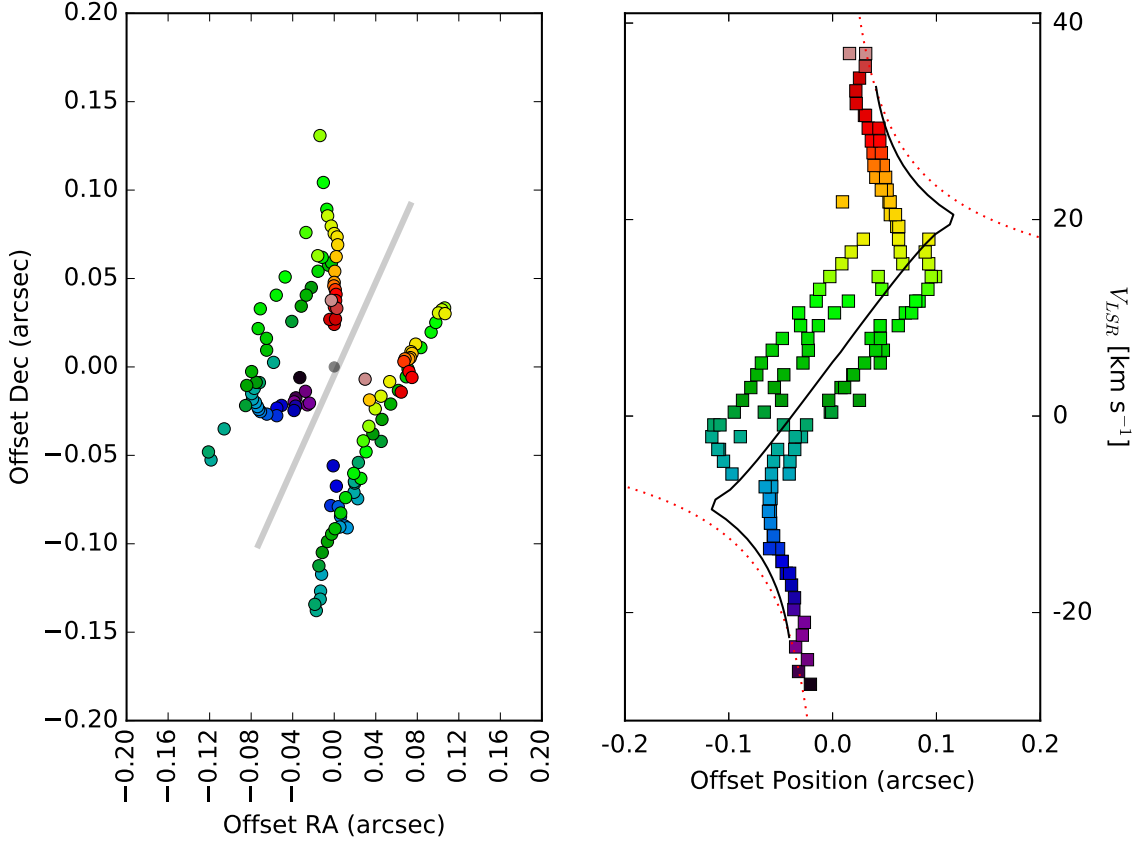


Figure 15. Results of the centroid-velocity analysis for the H₂O line. See Figure 13 for details. The model disk fit to these data was a very poor fit, so we have instead overlaid a model that is *not* a fit to the data with $15.5 M_{\odot}$, $r_{inner} = 17$ AU, and $r_{outer} = 66$ AU in the right panel. Note that the centroid positions do not extend as far from the source center as the unknown lines; this effect is a symptom of the blending of lines of sight in the centroid-based approach, since the H₂O line’s faintest emission can be seen extending to at least as great a distance from the central source as the unknown lines in the position-velocity diagrams.

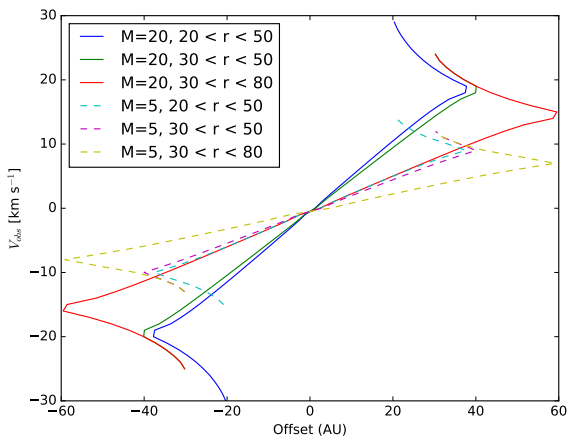


Figure 16. Plots of the predicted centroid rotation curves for different masses and inner and outer radial cutoffs. As discussed in Appendix E, this figure illustrates the ambiguity between the radial extent of the disk and the mass of the central source, since an $M = 5 M_{\odot}$ central source with a $20 < R < 50$ AU disk has the same slope in the inner part as a $M = 20 M_{\odot}$ source with a $30 < R < 80$ AU disk.

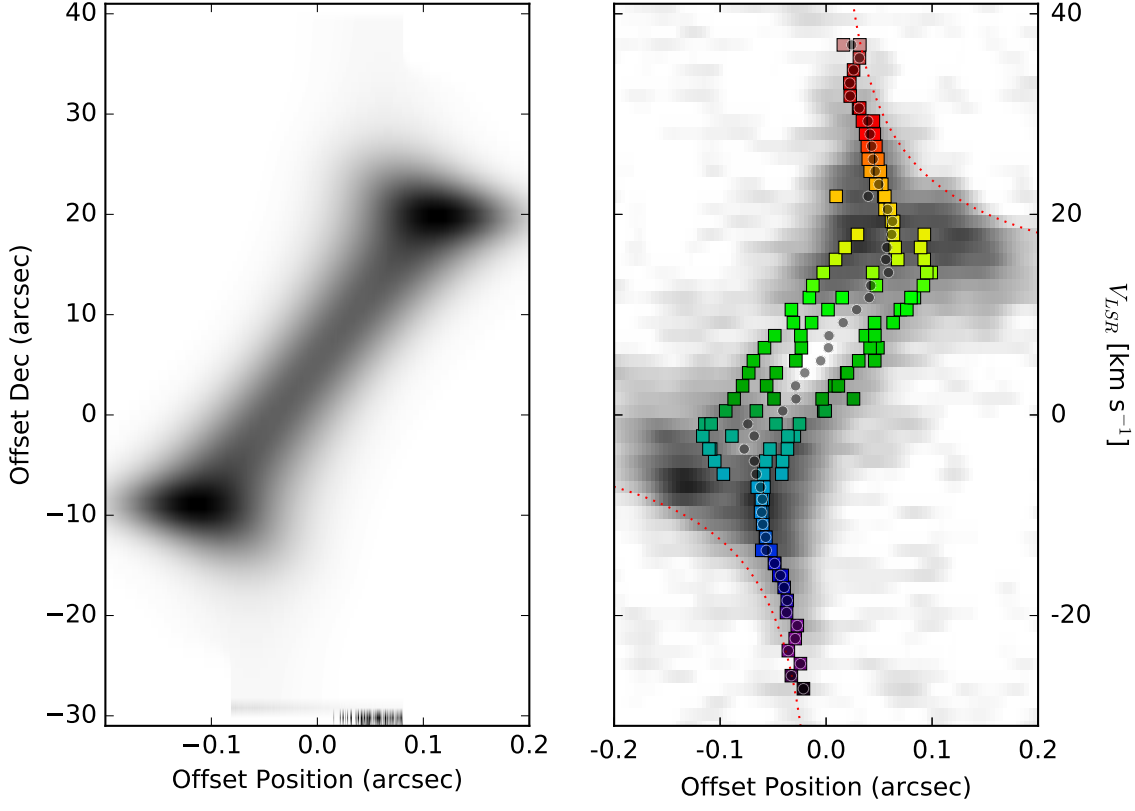


Figure 17. The edge-on disk model used to fit the centroid-of-velocity curves with $M = 15M_{\odot}$, $r_{in} = 25$ AU, and $r_{out} = 65$ AU (left) and the centroid-of-velocity measurements overlaid on the midplane position-velocity diagram of the H₂O line (right).

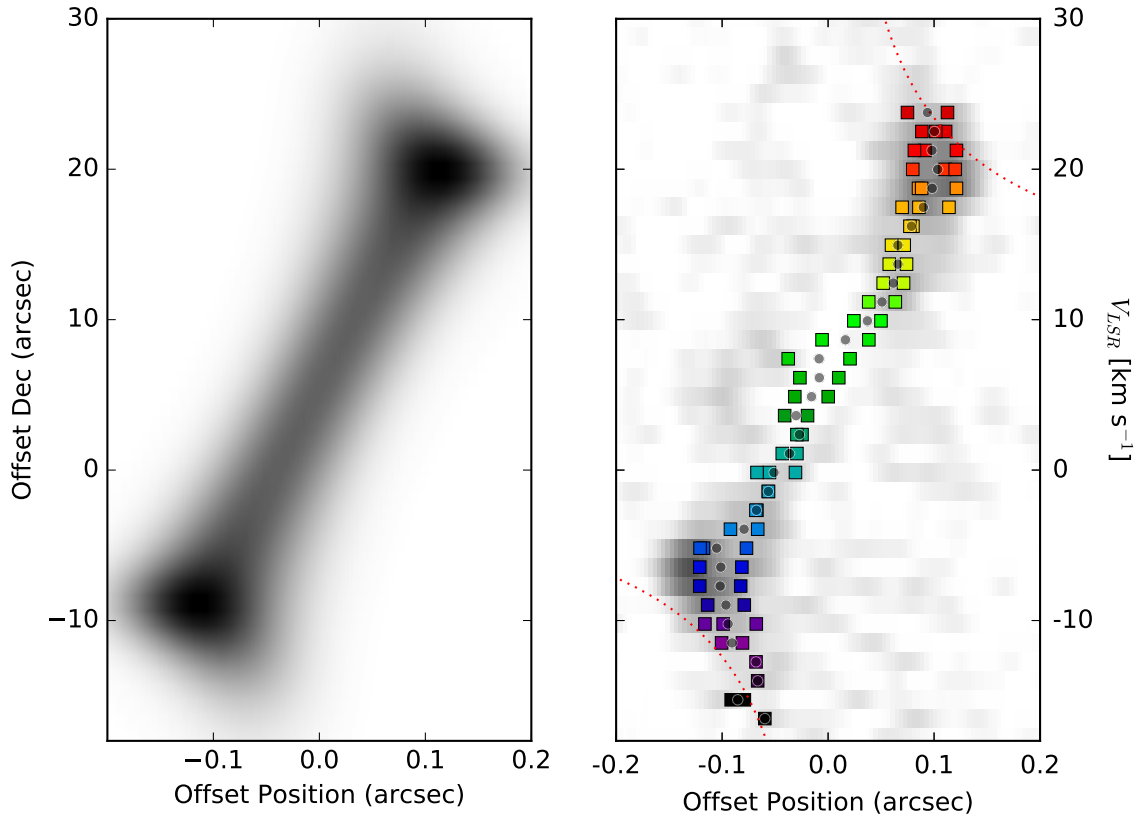


Figure 18. The edge-on disk model used to fit the centroid-of-velocity curves with $M = 15M_{\odot}$, $r_{in} = 25$ AU, and $r_{out} = 65$ AU (left) and the centroid-of-velocity measurements overlaid on the midplane position-velocity diagram of the U232.511 line (right).

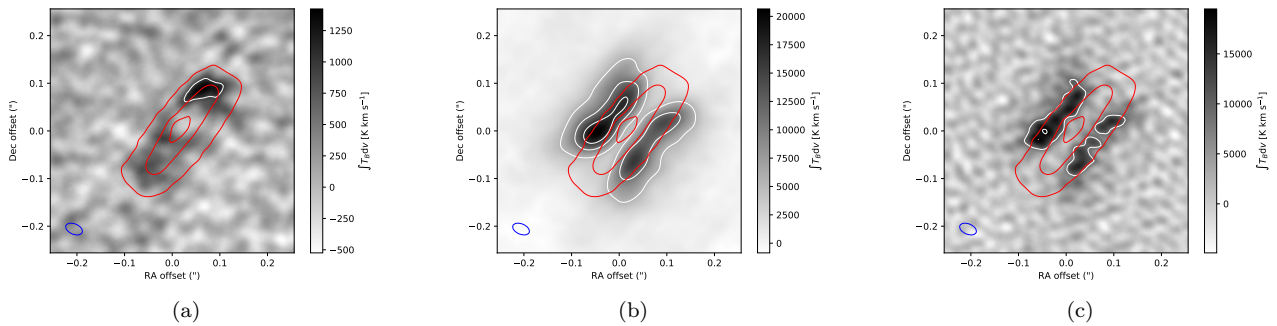


Figure 19. Moment-0 (integrated intensity) map of the U230.322 (left) and H₂O (middle, right) line with continuum overlaid in contours. Continuum contours from the robust -2 map are shown in red at levels of 50, 300, and 500 K. Contours of the line data are shown at 5, 10, and 15 σ . The left two figures are robust 0.5 weighted images, while the right is a robust -2 weighted image with higher resolution and poorer sensitivity. The U230.322 line is not detected in the robust -2 cubes.

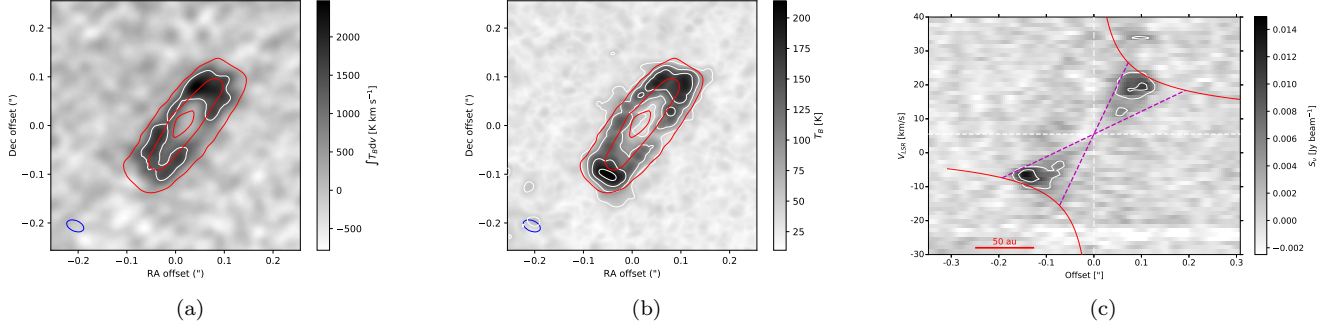


Figure 20. Moment 0 and peak intensity map of U232.511, similar to Figures 2 and 19. The rightmost panel shows a position-velocity diagram extracted from the disk midplane. The overlaid curve shows the Keplerian velocity profiles for a $15 M_{\odot}$ central source in red. The dashed magenta lines show the velocity curves at $r=30$ and 70 AU. In the left and right panels, contours of the line data are shown at 5 and 10σ , and in the center panel, they are at 50 , 100 , 150 , and 200 K.

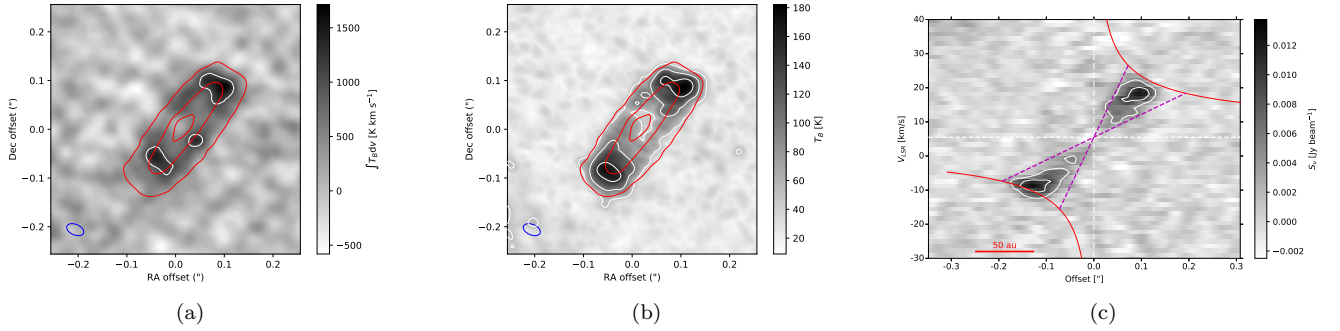


Figure 21. Moment 0 and peak intensity map of U217.980, similar to Figures 2 and 19. The rightmost panel shows a position-velocity diagram extracted from the disk midplane. The overlaid curve shows the Keplerian velocity profiles for a $15 M_{\odot}$ central source in red. The dashed magenta lines show the velocity curves at $r=30$ and 70 AU. In the left and right panels, contours of the line data are shown at 5 and 10σ , and in the center panel, they are at 50 , 100 , and 150 K.